arXiv:2404.16200v1 [astro-ph.GA] 24 Apr 2024

JWST MIRI detections of Hα and [O III] and direct metallicity measurement of the $z = 10.17$ lensed galaxy MACS0647−JD

Tiger Yu-Yang Hsiao [ID],[1,2,*] Javier Álvarez-Márquez [ID],[3,*] Dan Coe [ID],[2,1,4] Alejandro Crespo Gómez [ID],[3]
Abdurro'uf [ID],[1,2] Pratika Dayal [ID],[5] Rebecca L. Larson [ID],[6] Arjan Bik [ID],[7] Carmen Blanco-Prieto [ID],[3]
Luis Colina [ID],[3] Pablo Guillermo Perez Gonzalez [ID],[3] Luca Costantin [ID],[3] Carlota Prieto-Jiménez [ID],[3]
Angela Adamo [ID],[7] Larry D. Bradley [ID],[2] Christopher J. Conselice [ID],[8] Seiji Fujimoto [ID],[9,†]
Lukas J. Furtak [ID],[10] Taylor A. Hutchison [ID],[11,‡] Bethan L. James [ID],[2,4] Yolanda Jiménez-Teja [ID],[12,13]
Intae Jung [ID],[2] Vasily Kokorev [ID],[5] Matilde Mingozzi [ID],[2] Colin Norman [ID],[1,2] Massimo Ricotti [ID],[14]
Jane R. Rigby [ID],[11] Keren Sharon [ID],[15] Eros Vanzella [ID],[16] Brian Welch [ID],[11,14] Xinfeng Xu [ID],[17]
Erik Zackrisson [ID],[18,19] and Adi Zitrin [ID][10]

[1] Center for Astrophysical Sciences, Department of Physics and Astronomy, The Johns Hopkins University, 3400 N Charles St. Baltimore, MD 21218, USA
[2] Space Telescope Science Institute (STScI), 3700 San Martin Drive, Baltimore, MD 21218, USA
[3] Centro de Astrobiología (CAB), CSIC-INTA, Ctra. de Ajalvir km 4, Torrejón de Ardoz, E-28850, Madrid, Spain
[4] Association of Universities for Research in Astronomy (AURA), Inc. for the European Space Agency (ESA)
[5] Kapteyn Astronomical Institute, University of Groningen, P.O. Box 800, 9700AV Groningen, The Netherlands
[6] School of Physics and Astronomy, Rochester Institute of Technology, 84 Lomb Memorial Drive, Rochester, NY 14623, USA
[7] Department of Astronomy, Stockholm University, Oscar Klein Centre, AlbaNova University Centre, 106 91 Stockholm, Sweden
[8] Jodrell Bank Centre for Astrophysics, University of Manchester, Oxford Road, Manchester M13 9PL, UK
[9] Department of Astronomy, The University of Texas at Austin, Austin, TX 78712, USA
[10] Physics Department, Ben-Gurion University of the Negev, P.O. Box 653, Beér-Sheva 84105, Israel
[11] Observational Cosmology Lab, NASA Goddard Space Flight Center, Greenbelt, MD 20771, USA
[12] Instituto de Astrofísica de Andalucía, Glorieta de la Astronomía s/n, 18008 Granada, Spain
[13] Observatório Nacional - MCTI (ON), Rua Gal. José Cristino 77, São Cristóvão, 20921-400, Rio de Janeiro, Brazil
[14] Department of Astronomy, University of Maryland, College Park, 20742, USA
[15] Department of Astronomy, University of Michigan, 1085 S. University Ave, Ann Arbor, MI 48109, USA
[16] INAF−OAS, Osservatorio di Astrofisica e Scienza dello Spazio di Bologna, via Gobetti 93/3, I-40129 Bologna, Italy
[17] Department of Physics and Astronomy, Northwestern University, 2145 Sheridan Road, Evanston, IL, 60208, USA
[18] Observational Astrophysics, Department of Physics and Astronomy, Uppsala University, Box 516, SE-751 20 Uppsala, Sweden
[19] Swedish Collegium for Advanced Study, Linneanum, Thunbergsvägen 2, SE-752 38 Uppsala, Sweden

Submitted to ApJ

ABSTRACT

JWST spectroscopy has revolutionized our understanding of galaxies in the early universe. Covering wavelengths up to $5.3\,\mu$m, NIRSpec can detect rest-frame optical emission lines Hα out to $z = 7$ and [O III] to $z = 9.5$. Observing these lines in more distant galaxies requires longer wavelength spectroscopy with MIRI. Here we present MIRI MRS IFU observations of the lensed galaxy merger MACS0647−JD at $z = 10.165$. With exposure times of 4.2 hours in each of two bands, we detect Hα at 9σ, [O III] $\lambda5008$ at 11σ, and [O III] $\lambda4960$ at 3σ. Combined with previously reported NIRSpec spectroscopy that yields seven emission lines including the auroral line [O III] $\lambda4363$, we present the first direct metallicity measurement of a $z > 10$ galaxy: $12+\log(\text{O/H}) = 7.79 \pm 0.09$, or $0.13^{+0.02}_{-0.03}\,Z_\odot$. This is similar to galaxies at $z \sim 4 - 9$ with direct metallicity measurements, though higher than expected given the high specific star formation rate $\log(\text{sSFR / yr}^{-1}) = -7.4 \pm 0.3$. We further constrain the ionization parameter $\log(U) = -1.9 \pm 0.1$, ionizing photon production efficiency $\log(\xi_{\text{ion}}) = 25.3 \pm 0.1$,

Corresponding author: Tiger Hsiao, Javier Álvarez-Márquez
yhsiao17@jhu.edu, jalvarez@cab.inta-csic.es

and star formation rate $5.0 \pm 0.6 \, M_\odot$/yr within the past 10 Myr. These observations demonstrate the combined power of JWST NIRSpec and MIRI for studying galaxies in the first 500 million years.

1. INTRODUCTION

JWST was designed to study galaxies in the early universe (Gardner et al. 2023; Rigby et al. 2023), including the first galaxies composed of long-theorized Population III stars made of only the primordial elements hydrogen and helium formed in the Big Bang. Such pristine stars and galaxies would have no heavier elements and zero gas-phase metallicity.

While we have yet to find the elusive first-generation Pop III stars, we have measured the build-up of metals in galaxies over 13 billion of years of cosmic history. On average, gas-phase metallicity increases over time (decreases with redshift), increases with stellar mass (the mass-metallicity relation; e.g., Tremonti et al. 2004; Nakajima et al. 2023), and decreases with specific star formation rate (the Fundamental Metallicity Relation; e.g., Mannucci et al. 2010; Curti et al. 2020).

Ground-based telescopes have measured galaxy metallicities out to $z = 3.5$ based on measurements of restframe optical lines, including [O III] $\lambda 5008$, Hβ, and Hα. The fainter auroral line [O III] $\lambda 4363$, when detected, provides the most precise metallicity measurement based on the "direct" method of deriving the electron temperature T_e from the line flux ratio [O III] $\lambda 5008$ / $\lambda 4363$ (e.g., Peimbert 1967; Osterbrock 1989; Izotov et al. 2006; Kewley & Ellison 2008; Andrews & Martini 2013; Sanders et al. 2024). Stronger [O III] $\lambda 4363$ corresponds to higher temperatures T_e and lower metallicity.

JWST NIRSpec spectroscopy covering 0.6–5.3 μm (Jakobsen et al. 2022; Ferruit et al. 2022; Böker et al. 2023) has enabled direct metallicity measurements in galaxies out to $z \sim 9$ observed 500 Myr after the Big Bang. Most galaxies at $z \sim 4 - 9$ observed to date have metallicities ranging from 3% to 50% $Z_\odot$ (including direct method and strong line calibrations), or 12+log(O/H) = 7.2 – 8.4 (e.g., Curti et al. 2023; Nakajima et al. 2023; Boyett et al. 2023; Morishita et al. 2024). The most notable exception is the $z = 6.64$ strongly lensed galaxy LAP1 with very low metallicity < 0.4% $Z_\odot$, or 12+log(O/H) < 6.3 (Vanzella et al. 2023).

For more distant galaxies at $z > 9.5$, [O III] $\lambda 5008$ redshifts beyond NIRSpec's wavelength range, requiring the longer wavelength 5–28 μm coverage of MIRI (Rieke et al. 2015; Wright et al. 2015, 2023). MIRI is capable of detecting strong emission lines, such as Hβ, [O III] $\lambda 4960, \lambda 5008$ and Hα, in distant galaxies (Álvarez-Márquez et al. 2019) as recently demonstrated for the first time at $z > 9$ with Hα detections in the strongly lensed galaxy MACS1149-JD1 at $z = 9.11$ (Álvarez-Márquez et al. 2023a) and for the first time at $z > 10$ in the galaxy GHZ2/GLASS-z12, which is only weakly lensed, at $z = 12.33 \pm 0.02$ (Zavala et al. 2024).

The strongly lensed galaxy MACS0647$-$JD was discovered in HST imaging (Coe et al. 2013). Three lensed images JD1, JD2, and JD3 are observed with JWST NIRCam F200W AB mag 25.0, 25.4, and 26.2, respectively, for a total AB mag 24.2, making it the brightest $z > 10$ galaxy known (Hsiao et al. 2023a). The images are magnified by factors of $\sim$8.0, 5.3, and 2.2, based on lens modeling (Zitrin et al. 2015; Chan et al. 2017; Meena et al. 2023) and the observed flux ratios.

Hsiao et al. (2023a) reported that NIRCam imaging resolved MACS0647$-$JD as having two small stellar complexes A (JDA) and B (JDB) in a possible galaxy merger. The larger and brighter component A has an effective radius $r = 70 \pm 24$ pc and appears bluer, likely due to its young stellar population (~ 50 Myr old) and no dust. In contrast, the other component, JDB, is smaller, with a radius of $r = 20^{+8}_{-5}$ pc and is redder, likely due to an older stellar population ($\sim$100 Myr old) and mild obscuration ($A_V \sim 0.1$ mag). The dissimilar inferred star formation histories suggest the two components formed separately and are in the process of merging. Their projected separation is $\sim$400 pc (delensed). A possible third companion C, also triply-lensed, was identified $2''$ away ($\sim$3 kpc delensed).

JWST Cycle 1 NIRSpec prism spectroscopy confirmed the redshift $z = 10.17$ and revealed seven emission lines, including C III] $\lambda\lambda 1907, 1909$, [O II] $\lambda 3727$, [Ne III] $\lambda 3869$, [Ne III] $\lambda 3968$, Hδ $\lambda 4101$, Hγ $\lambda 4340$, and the auroral line [O III] $\lambda 4363$ (Hsiao et al. 2023b). Based the observed line ratios, Hsiao et al. (2023b) estimated the metallicity using various methods yielding values ranging from 6% to 20% $Z_\odot$. A direct metallicity measurement was not possible due to the lack of [O III] $\lambda 5008$.

This paper presents new MIRI Medium Resolution Spectrograph (MRS, Wells et al. 2015; Argyriou et al. 2023) and Mid-Infrared Imager Module (MIRIM, Bouchet et al. 2015; Dicken et al. 2024) observations of MACS0647–JD. The MRS spectroscopy yields detections of the [O III] $\lambda4960,\lambda5008$ and Hα emission lines, and the MIRI imaging shows the rest-frame optical structure of the galaxy merger. Our measured Hα flux provides a robust measurement of the star formation rate (SFR) and the ionizing photon production efficiency ($\xi_{\rm ion}$) when combined with existing rest-frame UV NIR-Cam photometry from Hsiao et al. (2023a). MIRI MRS in combination with NIRSpec prism spectroscopy provides the first ever measurement of the gas-phase metallicity (Z) using the "direct" method in a galaxy at a redshift $z > 10$. In addition to the metallicity, we are able to constrain key physical properties of the interstellar medium (ISM), including the electron temperature ($T_{\rm e}$) and the ionization parameter (U).

This paper is organized as follows: §2 describes the JWST/MIRI observations and data reduction. §3 presents the MRS 1D extracted spectra, emission line detections, and flux calculations. §4 details the main results and discusses them. §5 summarizes and concludes the paper.

Throughout, we use the AB magnitude system, which relates magnitude to flux in nanoJanskys via: AB mag $= 31.4 - 2.5\log(F_{\rm nJy})$ (Oke 1974; Oke & Gunn 1983). We adopt the *Planck* 2018 flat ΛCDM cosmology (Planck Collaboration et al. 2020) with $H_0 = 67.7$ km s^{-1} Mpc^{-1}, $\Omega_{\rm M} = 0.31$, and $\Omega_\Lambda = 0.69$, for which the universe is 13.8 billion years old, and $1'' \sim 4.2$ kpc at $z = 10.165$ observed 460 million years after the Big Bang. Where needed, we assume the Chabrier (2003) initial mass function (IMF). We quote metallicities $Z/Z_\odot$ relative to a solar abundance $12+\log(\mathrm{O/H}) = 8.69$ (Asplund et al. 2009). Lensing magnifications of 8.0 and 5.3 are adopted for JD1 and JD2, respectively (Hsiao et al. 2023a). Uncertainties from lensing effect are not propagated throughout the letter.

2. OBSERVATIONS AND DATA REDUCTION

JWST Cycle 2 program GO 4246 (PI: Abdurro'uf) observed MACS0647-JD simultaneously with MIRI MRS and MIRIM on February 11, 2024 (Figure 1). In this letter, we will only discuss the MIRI MRS data and save the imaging analysis for future work. The data are publicly available on MAST[1] and we provide reduced MRS data products on our website.[2]

2.1. *MIRI observations*

MRS observations have a FoV of $3.2''\times3.7''$ in channel 1. Our MRS pointing includes the three components (A, B, and C) of the JD1 lensed galaxy image. The observations were obtained in two MRS bands, SHORT and LONG, covering the 4.90–5.74 μm and 6.53–7.65 μm spectral ranges for channel 1, respectively. These spectral bands mainly target the Hβ and [O III] $\lambda4960,\lambda5008$, and the Hα bright optical emission lines, respectively. While the MRS observed JD1, MIRIM simultaneously imaged JD2 and an adjacent region with a FoV of $74''\times113''$ (Figure 1). MIRIM imaging was obtained in the F560W (5.0–6.3 μm) and F770W (6.6–8.7 μm) filters at the same time as the SHORT and LONG MRS observations, respectively. Total exposure times were 15194 seconds (4.2 hours) for each simultaneous MRS band + MIRIM filter. These were split among 4 dithers in a pattern optimized for extended sources. At each dither position, the 1.05-hour exposure consisted of 8 integrations of 19 groups of SLOWR1 readout.

Additional shallower observations were obtained of a nearby blank region 15$''$ to the west to measure MRS backgrounds. With single integrations and only 2 dithers, the total exposure times for these background observations were 15 minutes in each MRS band + MIRIM filter combination. The MRS background observations are not used in this paper, and the backgrounds are subtracted following a different methodology described below. We do include all MIRIM data, including the additional background exposures, in our image reductions. The on-source and background simultaneous MIRIM observations will be combined to generate the calibrated MIRIM images of filters F560W and F770W.

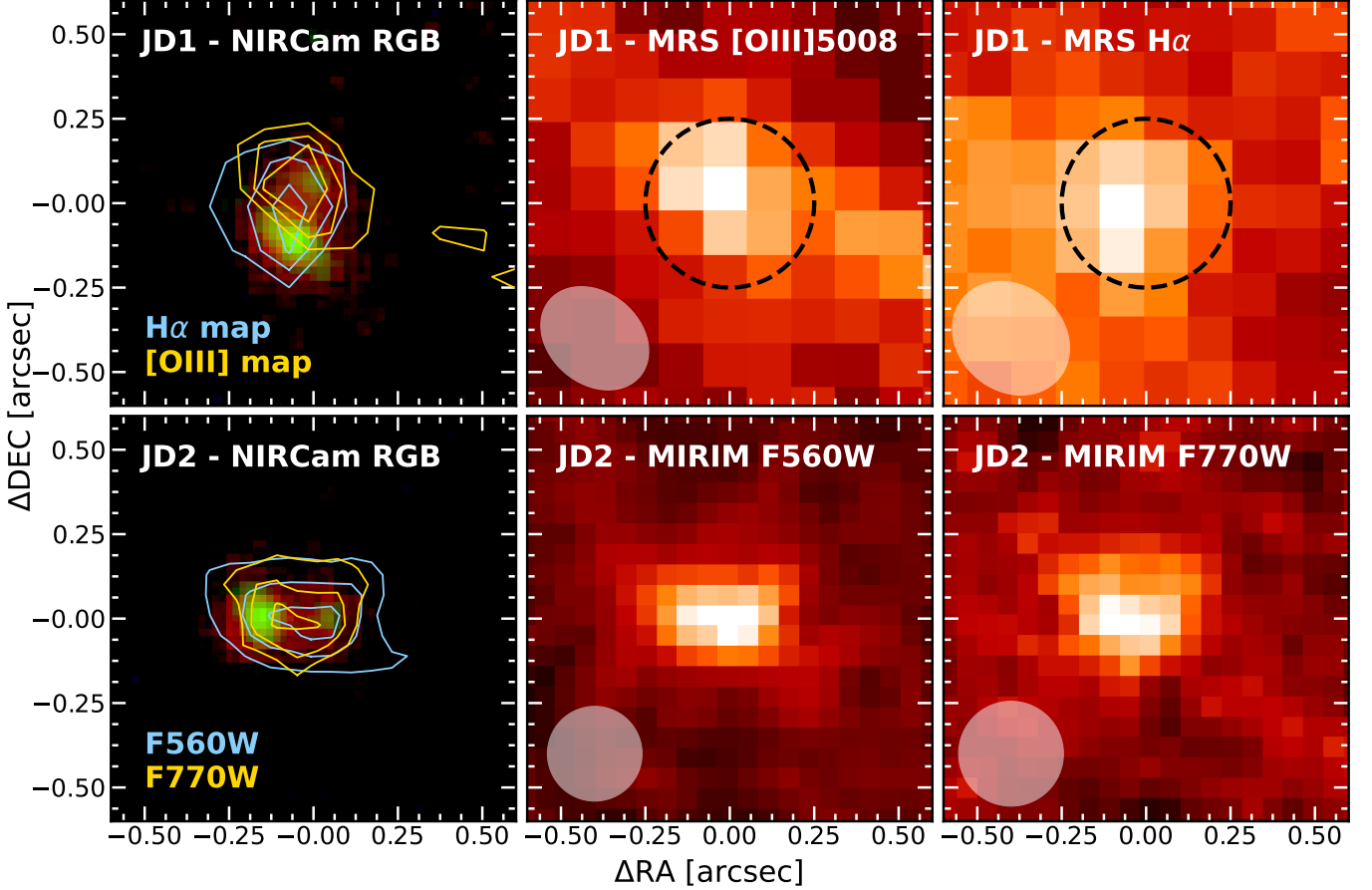### 2.2. *MIRI data calibration*

The MRS observations are processed with version 1.13.4 of the JWST calibration pipeline and context 1215 of the Calibration Reference Data System (CRDS). We follow the standard MRS pipeline procedure (Bushouse et al. 2024), with additional customized steps to improve the quality of the final MRS calibrated products (see Álvarez-Márquez et al. 2023b,a for details). These steps account for: (i) generation of a new bad and hot pixel mask, (ii) subtraction of the residual flux in regions of the detector that see no direct light to ensure a median count rate equal to zero and consistency in the flux calibrations, (iii) subtraction of 1/f noise (correlated noise in the vertical direction of the detector) using a smoothed function that additionally allows the removal of the residuals from shallow cosmic ray showers, (iv) generation and subtraction of a pixel-

Figure 1. JWST MIRI coverage of the MACS0647 field by GO 4246 (PI: Abdurro'uf) overlaid on the composite color image of JWST and HST. *Top left:* MIRI MRS IFU spectroscopy on the brightest lensed image, MACS0647−JD1, including all three clumps A, B, and C. All three components are observed in the FoV in all 4 dithers. *Bottom left:* The second brightest lensed image, MACS0647−JD2, is included in the MIRI imaging field of view. *Right:* Full image of the simultaneous MIRI imaging and MRS coverage. Note a bright 8th magnitude star lurks just below and right off the edge of the HST field of view. Two zoom insets show the JWST NIRCam images of JD1 and JD2.

by-pixel master detector background to correct any detector artifact and fringe residuals left after the standard calibrations, and (v) sigma clipping to mask the residuals of bright cosmic ray showers.

The compact dithers used in this program do not fully separate the emission of a point-like source in the various exposures and detector plane. This makes it impossible to use the on-source observations to generate a pixel-by-pixel master detector background clean of any emission from JD1. The dedicated background observations of this program have exposure times that are too short to perform a pixel-by-pixel detector background subtraction; they would inject significant noise into the on-source observations and reduce the SNR of the final calibrated cube.

So for step (iv) in this work, we follow a different approach than presented in the previous cited works. We have compiled MRS observations that are similar to MACS0647–JD: B14–65666, MACS1149–JD1 (Álvarez-Márquez et al. 2023a), and GNz11 from the MIRI European Consortium GTO programs (IDs 1284 & 1262) and the GO2 program (ID 2926). We have calibrated these observations following the same

procedure as MACS0647–JD1. The B14–65666 and GNz11 observations are used to generate the pixel-by-pixel master detector background of band SHORT, and MACS1149–JD1 observations are used for band LONG. These master backgrounds have been generated using a sigma-clipping median of all dithers, following Álvarez-Márquez et al. (2023b,a). We note these corrections do not significantly affect the background level, so any systematic differences in backgrounds between the datasets won't significantly affect the measured line fluxes.

The final 1SHORT and 1LONG 3D spectral cubes have a spatial and spectral sampling of 0.13" × 0.13" × 0.8 nm (Law et al. 2023), and a resolving power $R = \Delta\lambda/\lambda$ of about 3500 (85 km s^{-1}, Labiano et al. 2021; Jones et al. 2023).

The MIRIM observations are calibrated with version 1.13.4 of the JWST pipeline and context 1210 of the CRDS. In addition to the general procedure, our data calibration process includes additional steps to correct for striping artifacts and background gradients (see Álvarez-Márquez et al. 2023b; Pérez-González et al. 2024 for details). All of the MIRIM observations cover JD2, including both MRS on-source and back-

Figure 2. *Top row:* JD1 NIRCam F200W image (drizzled to 0.03″ pixels) and MIRI MRS line maps of [O III] λ5008 and Hα (0.13″ pixels) integrated within $\pm$100 km s^{-1} of the line peaks. Contours from these [O III] (yellow) and Hα (blue) line maps are overlaid on the NIRCam image of JD1. The dashed circle is used to measure flux shown in Figure 3. *Bottom row:* JD2 NIRCam F200W image and MIRIM F560W and F770W images (0.06″ pixels). Contours from F560W (blue) and F770W (yellow) line maps are overlaid on the NIRCam image of JD2. All data in each row are aligned and shown within an area 1.25″ × 1.25″. The center coordinates (RA, Dec) in degrees are (101.98225, 70.243302) for JD1 and (101.97128, 70.239721) for JD2. The JD1 centroid is also used for the aperture. PSF sizes are shown in the lower-left corners.

ground. Combining all MIRIM exposures, we generate final dithered F560W and F770W images with pixel sizes of 0.06″. We have generated effective point spread function (PSF) combining four stars within the MIRIM FoV. These PSFs present full width half maximum (FWHM) of 0.28″ and 0.31″, which correspond to 33% and 15% increase in the MIRI native spatial resolution due to the compact dithers pattern used in the MRS-MIRIM simultaneous observations (Libralato et al. 2024).

Finally, we correct the astrometry in the MIRIM and MRS observations. MIRIM images are aligned by measuring the centroid of two field stars with available GAIA DR3 (Gaia Collaboration et al. 2022) coordinates. As the MIRIM and MRS have been observed simultaneously, the offset correction for the MIRIM images is also implemented in the MRS 3D spectral cubes. The final uncertainty in the data-set alignment is less than a pixel in the MIRIM drizzle images (i.e., < 60 mas). Figure 2

shows the MRS [O III] λ5008 and Hα line maps of JD1 and the MIRIM F560W and F770W images of JD2. The line maps are generated by integrating the MRS cubes in the velocity range $-100 < v\,[\mathrm{km\,s^{-1}}] < 100$, taking as a reference the [O III] λ5008 and Hα emission line peaks derived by Gaussian line fitting (see Figure 3 and §3).

2.3. *NIRSpec and NIRCam ancillary data*

This letter also makes use of the NIRCam and NIRSpec observations of JWST Cycle 1 program GO 1433 (PI Coe). NIRCam imaging was obtained in 7 filters, F115W, F150W, F200W, F277W, F365W, F444W, and F480M spanning 1–5 μm. The NIRCam images were reduced by the STScI JWST pipeline and GRIZLI (Brammer et al. 2022). Photometry and the results were reported and discussed in Hsiao et al. (2023a). In this letter, we use the flux density of 317 nJy (Hsiao et al.

2023b) in F444W measured by GRIZLI for normalizing emission lines with NIRSpec prism (see §3.2).

NIRSpec multi-object spectroscopy (MOS) was performed in two observations (Obs 21 and Obs 23) using the microshutter assembly (MSA) with the low-resolution $R \sim 30 - 300$ prism spanning $0.6 - 5.3\,\mu m$ (Hsiao et al. 2023b). Obs 23 was executed with the standard 3-slitlet nods while Obs 21 was performed with single-slitlet mode. Both Obs 21 and Obs 23 observed JD1 and JD2. However, only Obs 21 JD2 targeted the center of MACS0647−JD, covering A+B (see Figure 1 in Hsiao et al. 2023b), while other observations mainly targeted JDA (including JD1A and JD2A). In this paper, we use emission line fluxes measured from the stacked spectrum (Hsiao et al. 2023b) as well as individually in Obs 21 JD2 as measured by Abdurro'uf et al. (2024) using PIXEDFIT code (Abdurro'uf et al. 2021, 2022). Ultimately, we find this choice does not significantly affect the results.

3. SPECTROSCOPIC MEASUREMENTS

3.1. *MIRI*

MRS spectroscopy has detected and spectrally resolved the rest-frame optical emission lines [O III] $\lambda 4960, \lambda 5008$ and Hα of JD1 (see Figures 2 and 3). JD1 rest-frame optical fluxes detected with MRS are spatially coincident with the A and B clumps identified in the NIRCam imaging covering the rest-frame UV emission (see Figure 2).

Clumps A and B of JD1 are not spatially resolved in the MRS 1SHORT and 1LONG observations, as their separation ($\sim 0.2''$, Hsiao et al. 2023a) is smaller than the PSF FWHM of the MRS channel 1 ($\sim 0.3'' \times 0.4''$, Argyriou et al. 2023). Thus in our analysis for this paper, we treat JD1 as an individual unresolved source. A small offset ($\sim 0.1''$) between [O III] $\lambda 5008$ and Hα is observed in the line maps presented in Figure 2. This offset could be interpreted as the combination of the low signal-to-noise ratio of the line maps, and the uncertainties derived from the astrometry correction ($< 60\,mas$) together with the MRS geometry distortion and wheel positioning repeatability ($\sim 40\text{-}50\,mas$; Patapis et al. 2024). The fainter companion clump C is within the MRS FoV but not detected in [O III] $\lambda 5008$ nor Hα.

3.1.1. *[O III]$\lambda 4960, \lambda 5008$ and Hα spectra and fluxes*

We extract the integrated [O III] $\lambda 4960, \lambda 5008$ and Hα 1D spectra of JD1 using a circular aperture of $0.25''$ radius in both MRS channels (see Figure 2). We also extract twelve background 1D spectra using the same sized aperture from random positions in the MRS FoV clean of source emission. We combine the twelve back-

ground spectra to generate the 1D median and standard deviation of the local background of each channel. The median background is compatible with zero in both cases, and the standard deviation is used as a 1σ error. The total [O III] $\lambda 4960, \lambda 5008$ and Hα spectra are shown in Figure 3, together with the 1σ error from the local background.

We model the [O III] $\lambda 5008$ and Hα emission line spectra with Gaussian functions plus a second-order polynomial to fit any residual background gradient (see Figure 3). The uncertainties on the derived emission line parameters, such as FWHM, flux, and redshift, are estimated by bootstrapping the spectra accordingly with the noise. The noise of the spectrum is measured as the RMS of the continuum surrounding the emission line. This noise is used to generate 1000 new spectra with random Gaussian noise added to the original spectrum before the lines are fit again. The final uncertainty is the standard deviation of all the individual measurements. In Table 1, we present [O III] $\lambda 5008$ and Hα line fluxes and Gaussian parameters based on these fits. The [O III] $\lambda 4960, \lambda 5008$ emission lines have been fitted together assuming a flux ratio of 2.98, the same FWHM and redshift.

We detect [O III] $\lambda 4960$ and [O III] $\lambda 5008$ with signal-to-noise ratios (SNRs) 3.6 and 10.7, and fluxes (75 ± 21)$\times 10^{-19}$ and (226 ± 21)$\times 10^{-19}$ erg s^{-1} cm^{-2}, respectively. Hα is detected with SNR 9.0 and flux (90 ± 10)$\times 10^{-19}$ erg s^{-1} cm^{-2}. The line fluxes have been corrected for aperture losses, assuming that the JD1 emission is spatially unresolved. The redshift calculated from the location of the peak of the Gaussian fit is 10.1644 ± 0.0005 and 10.1659 ± 0.0004 for [O III] $\lambda 5008$ and Hα respectively. The [O III] $\lambda 5008$ and Hα lines have intrinsic FWHM of 191 ± 19 km s^{-1} and 127 ± 19 km s^{-1}, respectively, after correcting for the instrumental line broadening (Labiano et al. 2021), and an velocity offset of 39 ± 20 km s^{-1}. The redshift offset and FWHM difference between the two lines are due to the asymmetry of the [O III] $\lambda 5008$ emission line, which blueshifts the peak location and broadens the profile of the Gaussian fit. The [O III] $\lambda 5008$ line could alternatively be modeled as a sum of two Gaussians, with the main component having the same redshift and FWHM as Hα. Analysis of the [O III] $\lambda 5008$ line profile asymmetry is outside the scope of this paper and will be presented in Álvarez-Márquez in prep.

Fainter emission lines covered by the 1SHORT and 1LONG wavelength ranges were not detected. Assuming Case B recombination, we expect a flux ratio Hα / Hβ = 2.86 and an Hβ flux $\sim 3 \times 10^{-18}$ erg s^{-1} cm^{-2}. Thus we should only expect SNR ~ 1.5
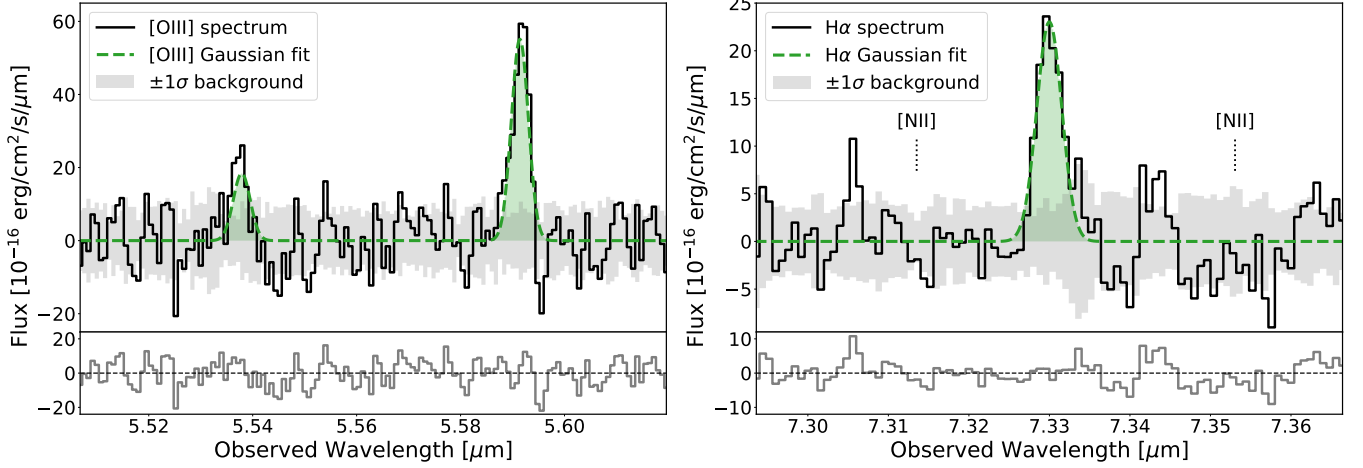
Figure 3. MIRI MRS spectra of [O III] λ4960,λ5008 and Hα observed at $z = 10.165$. *Left:* [O III] λ5008 and [O III] λ4960 spectra in black measured within the circular aperture shown in Figure 2. Uncertainties are shown in shaded gray. A single Gaussian (green) is well fit to the [O III] λ5008 line; that same fit is shown for the [O III] λ4960 line after reducing the flux by a factor of 2.98. Fit residuals are shown in the bottom plot. *Right:* Hα spectrum fit to a single Gaussian. Vertical dashed lines show the wavelengths of the weaker undetected lines [N II] λ6550,λ6585 that are well separated in wavelength and thus do not contribute to Hα λ6563.

in MRS 1SHORT (which is slightly less sensitive than 1LONG) given the 1σ flux uncertainties $\sim 2\times10^{-18}$ $\mathrm{erg\,s^{-1}\,cm^{-2}}$ at the Hβ rest-frame wavelength 4863Å near [O III] λ4960,λ5008. Still fainter lines eluding detection include [N II] λ6550,λ6585 and [S II] λ6718,λ6733 with 1σ uncertainty $\sim10^{-18}$ $\mathrm{erg\,s^{-1}\,cm^{-2}}$, or 3σ upper limits $\sim3\times10^{-18}$ $\mathrm{erg\,s^{-1}\,cm^{-2}}$.

3.2. *NIRSpec spectroscopy normalized to MIRI MRS*

We assume our MIRI MRS line flux measurements are the total values for JD1 A+B, given the complete coverage with the IFU and the aperture loss corrections we applied to our 0.25″ aperture. We cannot say the same for our NIRSpec MSA line fluxes since the slits do not fully cover JD1 A+B, and our slit loss corrections are uncertain. The JWST pipeline corrects for slit losses assuming either a point source or uniform illumination; we choose the point source option. More robust slit loss estimates would require modeling the two extended sources, as in de Graaff et al. (2023).

In Hsiao et al. (2023b), we measured NIRCam photometry within rectangular apertures matched to the NIRSpec MSA slits. This yielded 133 ± 3 nJy in F444W after renormalizing to the JD1 magnification $\mu = 8$. We compared this to the JD1 NIRCam F444W flux 317 ± 8 nJy measured in a larger aperture ($r = 0.25″$), estimating a flux loss factor of 2.4. However, this technique assumes uniform transmission through the slits, not accounting for slit losses.

Here, we integrate the NIRSpec prism spectra over the F444W filter, measuring 105 nJy for the stacked spectrum (with JD1 magnification $\mu = 8$), yielding a flux loss factor of 3.0. Thus we multiply our NIRSpec line flux measurements by a factor of 3 to correct for slit losses and apply other factors as needed to correct for magnification. We use updated line flux measurements presented in Abdurro'uf et al. (2024) that are similar to those presented in Hsiao et al. (2023b) for the stacked spectrum.

Based on this normalization, we estimate Hα / Hγ $= 5.5 \pm 0.7$. We adopt this normalization as fiducial in our analysis. This is consistent with the expected ratio Hα / Hγ $= 6.11$ (5.79) for Case B recombination at $T = 10000\,\mathrm{K}$ (20000 K) (e.g., Dopita & Sutherland 2003; Groves et al. 2012). We also consider an alternative analysis fixing the line ratio to Hα / Hγ $= 6.11$ (assuming no dust).

In addition, we perform the same procedure with the individual NIRSpec prism observation (Obs 21 JD2) that is best centered on A+B (though not fully including both), perhaps better corresponding to the centroid of the line emission combined from both clumps A and B (see Hsiao et al. 2023b and Abdurro'uf et al. 2024). This observation may be more representative of MACS0647–JD as a whole. Our analyses of the NIRSpec and MIRI data assume all the emission comes from a single source since we do not spatially resolve A and B with these observations.

Table 1. MIRI MRS measured emission line fluxes for MACS0647−JD1.

Emission Line	Rest wavelength Å	Observed wavelength μm	Redshift z	Observed Flux[a] $10^{-19}\,\mathrm{erg/s/cm^2}$	Observed FWHM $\mathrm{km\,s^{-1}}$	Intrinsic FWHM $\mathrm{km\,s^{-1}}$
[O III]	4960.30	5.5379 [b]		75 [c]		
[O III]	5008.22	5.5915 ± 0.0002	10.1644 ± 0.0004	226 ± 21	206 ± 21	191 ± 19
Hα	6564.62	7.3300 ± 0.0002	10.1659 ± 0.0003	90 ± 10	150 ± 19	127 ± 16

[a] JD1 line fluxes are not corrected for lensing magnification ($\mu = 8$).

[b] [O III] $\lambda 4960$ wavelength, redshift, and FWHM fixed to those of [O III] $\lambda 5008$.

[c] [O III] $\lambda 4960$ flux assigned [O III] $\lambda 5008$ flux divided by 2.98.

Table 2. Emission line ratios and physical properties estimated for MACS0647−JD.

	NIRSpec prism		Normalized to Hα/Hγ=6.11	
	Stack[a]	Obs 21 JD2	Stack	Obs 21 JD2
Emission Line Ratios				
[O III] $\lambda 5008$ / $\lambda 4363$	40 ± 5	48 ± 16	44 ± 5	32 ± 10
O32 = [O III] $\lambda 5008$ / [O II] $\lambda 3727$	17 ± 2	13 ± 2	19 ± 1	8 ± 1
Hα / Hγ	5.5 ± 0.7	3.8 ± 0.6	6.11 (fixed)	
R3 = [O III] $\lambda 5008$ / Hβ[b]	6.9 ± 1.0			
Physical Properties				
12+log(O/H)[c]	7.79 ± 0.09	7.90 ± 0.15	7.84 ± 0.09	7.74 ± 0.14
$Z/Z_\odot$	$0.13^{+0.03}_{-0.02}$	$0.16^{+0.07}_{-0.05}$	0.14 ± 0.03	$0.11^{+0.04}_{-0.03}$
$\log(U)$	-1.9 ± 0.1	-2.0 ± 0.1	-1.9 ± 0.1	-1.7 ± 0.1
SFR ($M_\odot\,\mathrm{yr^{-1}}$)	5.0 ± 0.6			
$\log(\xi_\mathrm{ion})$	25.3 ± 0.1			
T_e([OIII])(K)	17000 ± 1000	15000 ± 2000	16000 ± 1000	19000 ± 3000

[a] We adopt this configuration as fiducial values throughout the letter.

[b] Hβ is estimated as Hα / 2.74

[c] Estimated using PYNEB. Other methods gave similar results (see §4.3).

4. RESULT AND DISCUSSION

4.1. SFR and ξ_ion

Given this nearly unprecedented measurement of Hα at $z > 10$ (see also Zavala et al. 2024), we can directly measure the recent star formation rate (SFR) and ionizing photon production efficiency ξ_ion of MACS0647−JD.

Based on the total measured JD1 Hα line flux $(9 \pm 1) \times 10^{-18}\,\mathrm{erg\,s^{-1}\,cm^{-2}}$, and correcting for magnification $\mu \approx 8$, we estimate an intrinsic luminosity $L_\mathrm{H\alpha} = (1.6 \pm 0.2) \times 10^{42}\,\mathrm{erg\,s^{-1}}$. Adopting an SFR conversion factor of 3.2×10^{-42} suitable for high-redshift galaxies (Reddy et al. 2018), we estimate SFR = $5.0 \pm 0.6\,M_\odot \mathrm{yr^{-1}}$, as-

suming zero escape fraction, no dust attenuation, and a Chabrier (2003) IMF. Note that a factor of 4.2×10^{-42} from Kennicutt (1998) would overestimate the SFR for a high-z galaxy with lower metallicity. This is consistent with previous estimates based on JWST NIRCam SED fitting ($\sim 4 - 10\,M_*$/yr Hsiao et al. 2023a,b). We note that it is higher than the estimates of SFR = 1.4 ± 0.2 from NIRSpec prism spectroscopy including Hγ (Hsiao et al. 2023b), since NIRSpec observations mainly targeted A and it is not corrected for flux losses (see also §3.2).

The ionizing photon production efficiency can be expressed as $\xi_{\rm ion} = \dot{N}_{\rm ion}/L_\nu^{\rm UV}$, where $L_\nu^{\rm UV}$ is the UV luminosity and $\dot{N}_{\rm ion}$ stands for the production rate of hydrogen-ionizing photons. We use Hα to derive $\dot{N}_{\rm ion}$ of $(1.2 \pm 0.1) \times 10^{54}$ s^{-1}, where $\log(L_{\rm H\alpha}) = \log(\dot{N}_{\rm ion}) - 11.87$, assuming zero escape fraction and no dust. This value should be treated as a lower limit since a $z \sim 10.165$ galaxy likely has some non-zero escape fraction. Combined with our measured and demagnified UV luminosity (Hsiao et al. 2023b) for MACS0647−JD of $(5.8 \pm 1.0) \times 10^{28}$ erg s^{-1} Hz^{-1} (corresponding to $M_{UV} = -20.3 \pm 0.2$; where $M_{UV} = -2.5\log L_\nu^{\rm UV} + 51.6$; Oke & Gunn 1983), we estimate an ionizing photon production efficiency $\xi_{\rm ion} = \dot{N}_{\rm ion}/L_\nu^{\rm UV} = 2.0 \pm 0.5 \times 10^{25}$ erg^{-1} Hz, or $\log(\xi_{\rm ion}) = 25.3 \pm 0.1$. This is consistent with the previous estimate $\log(\xi_{\rm ion}) = 25.2 \pm 0.2$ based on NIRSpec prism spectroscopy without Hα (Hsiao et al. 2023b), and it is similar to the canonical value of 25.2 (Robertson et al. 2013). It is also similar to the value recently reported for GHZ2/GLASS-z12 at $z = 12.34$ (Zavala et al. 2024). This aligns with predictions for high-redshift galaxies ($z > 8$), especially in younger ($\lesssim 10^8$ yr) and lower-metallicity ($Z \lesssim Z_\odot$) galaxies (e.g., Schaerer 2003; Wilkins et al. 2016). However, other recent JWST studies find somewhat higher $\log(\xi_{\rm ion})$ between 25.4 and 26.0 for high-redshift ($7 < z < 11$) galaxies (e.g., Tang et al. 2023; Bunker et al. 2023; Fujimoto et al. 2023; Álvarez-Márquez et al. 2023a), as shown in Figure 4. Recent studies indicate that fainter galaxies tend to have higher $\xi_{\rm ion}$, while brighter galaxies exhibit lower $\xi_{\rm ion}$ (e.g., Jung et al. 2023; Fujimoto et al. 2023; Atek et al. 2024). Our $\xi_{\rm ion}$ measurement for MACS0647−JD falls within the expected range for galaxies of similar UV luminosity ($M_{\rm UV} \sim 20.3$).

4.2. *Ionization parameter* $\log(U)$

The line ratio O32 = [O III] $\lambda5008$ / [O II] $\lambda3727$ has long been used (e.g., Hicks et al. 2002; Papovich et al. 2022) as a diagnostic for the ionization parameter $\log(U)$. We measure a ratio of O32 = 17 ± 2, which corresponds to $\log(U) = -1.9 \pm 0.1$ adopting the relation from Papovich et al. (2022) or $\log(U) = -2.0 \pm 0.1$ adopting the relation from Díaz et al. (2000). Note that these relations are not accounting the low-metallcitiy in MACS0647−JD. We also analyze our observed line ratios to estimate the ionization parameter using HII-CHI-MISTRY version 5.22[3] (Pérez-Montero 2014), which yields $\log(U) = -1.7 \pm 0.1$, adopting Binary Population and Stellar Synthesis (BPASS) templates (Stanway &

---

[3] https://home.iaa.csic.es/~epm/HII-CHI-mistry-opt.html
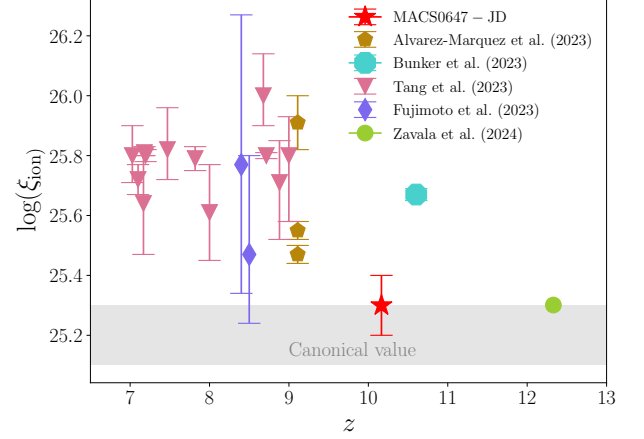
Figure 4. The comparison of $\log(\xi_{\rm ion})$ of MACS0647−JD to the previous estimates at $z \gtrsim 7$. Brown pentagons are MACS1149-JD1 at $z = 9.11$ (Álvarez-Márquez et al. 2023a). The turquoise hexagon is GNz11 at $z = 10.603$ (Bunker et al. 2023). Pink triangles represent galaxies at $7 < z < 9$ (Tang et al. 2023). Violet diamonds are median values of NIRCam and HST- selected galaxies at $8 < z < 9$ (Fujimoto et al. 2023). The green point shows GHZ2/GLASS-z12 at $z = 12.33$ (Zavala et al. 2024). The canonical value of 25.2 ± 0.1 is shown as the gray shaded region (Robertson et al. 2013).

Eldridge 2018) and constraints for Star-Forming Galaxies in HII-CHI-MISTRY. All of the $\log(U)$ values derived above are consistent within uncertainties. The various values in Table 2 are also consistent within their uncertainties. These also agree with the previous estimate $\log(U) = -1.9 \pm 0.2$ using Ne3O2 to estimate O32 (Hsiao et al. 2023b) before [O III] had been measured in this work.

Our measurement for MACS0647−JD is similar to the value $\log(U) = -1.8 \pm 0.3$ measured for GHZ2/GLASS-z12 at $z = 12.33$ (Castellano et al. 2024; Zavala et al. 2024) and $\log(U) = -2.2 \pm 0.9$ measured for GN-z11 at $z = 10.60$ (Bunker et al. 2023). These and other similar measurements of $\log(U) \sim -2$ for high-redshift galaxies reveal strong ionization parameters, comparable to the more starbursting environments we see at low-redshift, but overall higher than the non-star forming galaxies (e.g., Kewley & Dopita 2002; Mingozzi et al. 2024).

4.3. *Direct Metallicity*

Based on the measured line fluxes of [O III] $\lambda5008$ from MIRI MRS and the auroral line [O III] $\lambda4363$ from NIRSpec, we can obtain a direct metallicity measurement based on electron temperature. We measure the line flux ratio [O III] $\lambda5008$/[O III] $\lambda4363 = 40 \pm 5$. Based on this flux ratio, we derive the electron temperature of the high-ionization zone $T_{\rm e}([{\rm O\,III}]) = 17000 \pm 1000$ K using
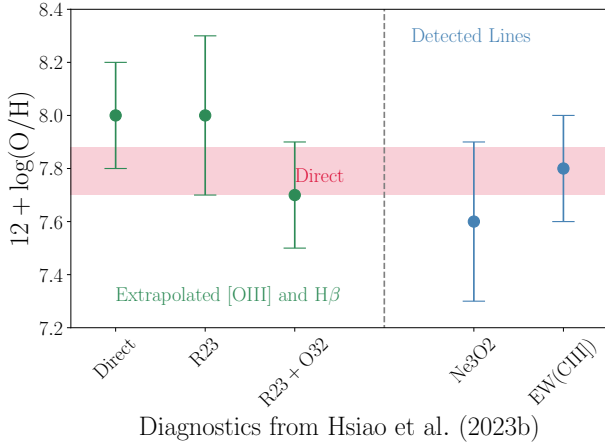
Figure 5. MACS0647–JD metallicity measured using the direct-T_e method in this paper (crimson band) compared to the previous estimates using different indirect diagnostics in Hsiao et al. (2023b): green data points included estimated line fluxes for [O III] and Hβ, while the blue data points relied on detected lines only. Note that for the "direct" method in the x-axis, Hsiao et al. (2023b) extrapolated [O III] and Hβ from detected lines.

the PYNEB (Luridiana et al. 2015) task `getTemDen`. We also find a similar value of $\sim 17000\,\mathrm{K}$ using the equation 4 in Nicholls et al. (2020). We then apply the relation $T_{\mathrm{e}}(\mathrm{[O\,II]}) = 0.7 \times T_{\mathrm{e}}(\mathrm{[O\,III]}) + 3000\,\mathrm{K}$ (Campbell et al. 1986) to estimate the low-ionization zone gas temperature $T_{\mathrm{e}}(\mathrm{[O\,II]}) = 15000 \pm 1000\,\mathrm{K}$, and the $\mathrm{O^{+}/H}$ ionic abundance. Adding the oxygen abundances from both zones, we derive a metallicity $12 + \log(\mathrm{O/H}) = 7.79 \pm 0.09$, or $13^{+2}_{-3}\%\,Z_{\odot}$. We adopt this as our fiducial result. We also utilize HII-CHI-MISTRY to estimate a metallicity of $12+\log(\mathrm{O/H}) \sim 7.56 \pm 0.12$, corresponding to $\sim (7^{+3}_{-1})\%\,Z_{\odot}$.

These results do not vary significantly for density values n_{e} between 300 and 3000 cm^{-3}, the range measured for MACS0647–JD in our companion paper by resolving the [O II] doublet (Abdurro'uf et al. 2024).

The results also do not depend strongly on our choices for NIRSpec line fluxes and normalization (§3.2). Table 2 presents the results with metallicity $12+\log(\mathrm{O/H})$ ranging from 7.7 – 7.9 (11–16% $Z_{\odot}$) and electron temperature ranging between $15000 - 19000\,\mathrm{K}$.

Our direct metallicity measurement is consistent with the range $\sim 6 - 20\%\,Z_{\odot}$ estimated by Hsiao et al. (2023b) using different approaches based on lines including [O III] $\lambda 4363$ and estimates for [O III] $\lambda 5008$ and Hβ. We compare these estimates in Figure 5.

In Figure 6, we plot direct metallicity versus strong line ratios for MACS0647–JD and galaxies at $z \sim 2$ – 9 from Sanders et al. (2024). Overall, the relation

between the direct metallicity and different strong line ratios of MACS0647–JD is consistent with galaxies at lower redshift $z \sim 2 - 9$.

The MACS0647–JD metallicity $12+\log(\mathrm{O/H}) = 7.8 \pm 0.1$ is similar to most direct metallicity measurements from JWST for galaxies at $z \sim 4$ – 9 (e.g., Nakajima et al. 2023; Heintz et al. 2023; Curti et al. 2023; Morishita et al. 2024). In Figure 7, we plot metallicity vs. stellar mass for these galaxies, including $\log(M/M_{\odot}) = 8.1 \pm 0.3$ measured for MACS0647–JD by Hsiao et al. (2023b) using SED fitting. Given the current limited (and potentially biased) sample of galaxies with direct metallicity measurements, we do not detect strong trends with redshift over the billion years from $z \sim 4$ to 10 or stellar mass from 10^7 to $10^{10}\,M_{\odot}$. If these trends were stronger, we would expect MACS0647–JD to have one of the lowest metallicities given its relatively low stellar mass and highest redshift among these galaxies. But we find its metallicity is roughly average compared to the others at $z \sim 4 - 10$. This is likely due to a combination of intrinsic scatter and measurement uncertainties.

In the bottom panel of the same figure, we also show a comparison with theoretical results including those from semi-analytic models (Dayal et al. 2022), semi-numerical models (Ucci et al. 2023) and hydrodynamic simulations (Wilkins et al. 2023; Marszewski et al. 2024). Although about 0.3 dex higher than the average predicted relation at $z \sim 10$, MACS0647–JD's metallicity falls within the range predicted by the ASTRAEUS framework (Ucci et al. 2023) and is about 0.3 dex higher than that predicted by FLARES (Wilkins et al. 2023). Our measurement is in perfect accord with recent results from semi-analytic models tuned against the latest ALMA and JWST data sets (DELPHI; Dayal et al. 2022) and the state-of-the-art hydrodynamic simulations (FIRE-2; Marszewski et al. 2024), although these predict extremely different slopes for the mass-metallicity relation. These demarcate the impact of different methodologies and assumptions (metal production, dispersal, the impact of feedback on the gas and metal content, to name a few) on determining the mass-metallicity relation at these early epochs.

In Figure 8, we plot the Fundamental Metallicity relation where MACS0647–JD is again consistent with high redshift ($z \sim 4 - 9$) galaxies with direct metallicity measurements. Given the relatively high specific star formation rate $\log(\mathrm{sSFR} / \mathrm{yr}^{-1}) = -7.4 \pm 0.3$ for this low-mass system, the ASTRAEUS model (Ucci et al. 2023) predicts a lower metallicity $12+\log(\mathrm{O/H}) \leq 7.5$ suppressed by outflows. But the simulation expectations are close given our uncertainties on $\log(\mathrm{sSFR})$. The redshift-
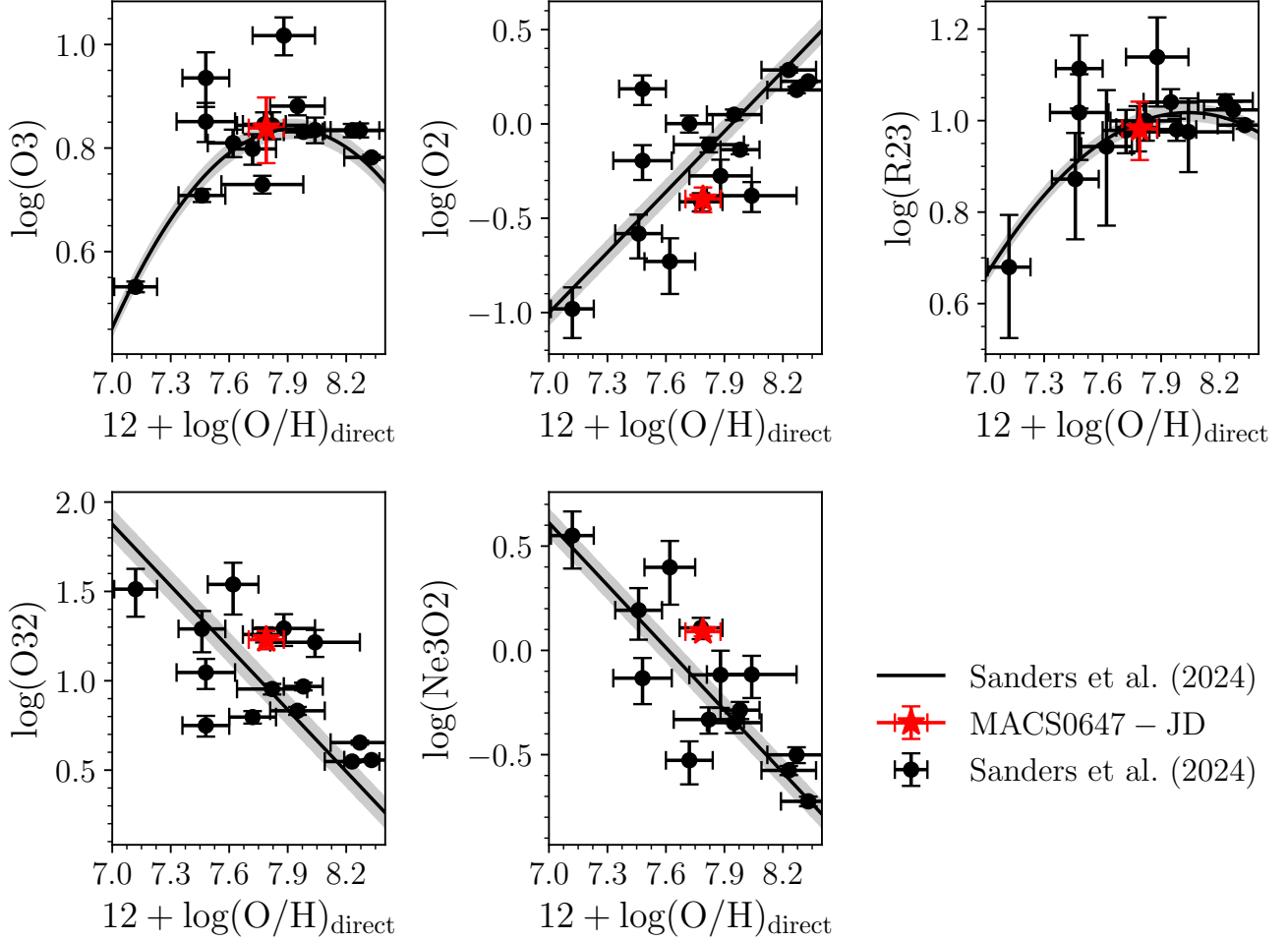
Figure 6. MACS0647−JD metallcity using the direct-T_e method plotted in red against various strong line ratios measured in Hsiao et al. (2023b). Black points show similar measurements for galaxies at $z \sim 2-9$ from Sanders et al. (2024). The line flux ratios are O3=[O III] $\lambda5008$/Hβ; O2=[O II] $\lambda3727$/Hβ; R23=([O III] $\lambda4960,\lambda5008$+[O II] $\lambda3727$)/Hβ; O32=[O III] $\lambda5008$/[O II] $\lambda3727$; and Ne3O2=[Ne III] $\lambda3869$/[O II] $\lambda3727$.

dependent extrapolated expectations from Tortora et al. (2022) are similarly close. Comparing with lower-redshift relations, we find MACS0647−JD's metallicity is at the low end of $z \sim 1.5 - 3.5$ observationally-inferred expectations from Sanders et al. (2021), while more galaxies at $z > 10$ with direct metallicity with more precise determinations of SFR and stellar mass are required for more detail discussion.

5. CONCLUSIONS

In this letter, we report MIRI spectroscopic observation of the triply-lensed galaxy merger MACS0647−JD at $z = 10.165$. We detect the rest-frame optical emission lines Hα, [O III] $\lambda5008$, and [O III] $\lambda4960$ and measure line fluxes (23 ± 2) and $(9\pm1) \times 10^{-18}$ erg s^{-1} cm^{-2} for [O III] $\lambda5008$ and Hα, respectively, with a line flux ratio 2.5 ± 0.4. Analyzed jointly with NIRSpec prism line

flux measurements presented in Hsiao et al. (2023b), including the auroral line [O III] $\lambda4363$, we present the first direct metallicity measurement of a $z > 10$ galaxy: $12+\log(\mathrm{O/H}) = 7.79 \pm 0.09$, or $0.13^{+0.02}_{-0.03} Z_\odot$. We also measure the ionization parameter $\log(U) = -1.9 \pm 0.1$, ionizing photon production efficiency $\log(\xi_\mathrm{ion}) = 25.3 \pm 0.1$, and SFR $5.0 \pm 0.6 M_\odot$/yr within the past 10 Myr.

Given the stellar mass $\log(M/M_\odot) = 8.1 \pm 0.3$ (Hsiao et al. 2023b) and specific star formation rate $\log(\mathrm{sSFR} / \mathrm{yr}^{-1}) = -7.4 \pm 0.3$, we might have expected a lower metallicity $12+\log(\mathrm{O/H}) \sim 7.2$, or $\sim3\% Z_\odot$ (Ucci et al. 2023). Instead, the MACS0647−JD metallicity is similar to galaxies at $z \sim 4 - 9$ with direct metallicity measurements (e.g., Nakajima et al. 2023; Curti et al. 2023; Morishita et al. 2024; Heintz et al. 2023). With a delensed F200W AB mag 27.2 ($M_{UV} = -20.3$), MACS0647−JD may be a typical and representative

Figure 8. Similar to Figure 7 but the fundamental-metallicity relation. MACS0647−JD (this work) determined using direct T_e method is shown in the red star. We compare MACS0647−JD with some previous high-redshift direct metallicity measurements from Nakajima et al. (2023, orange Xs) at $4 < z < 10$ and Morishita et al. (2024, tiffany green triangles) at $3 < z < 9.5$. Galaxies at $z > 7$ are specifically marked with magenta circles. We also compare MACS0647−JD to Astraeus (Ucci et al. 2023) simulation predictions at $z = 10.165$, which is shown using the steel-blue shaded region. We also show observationally inferred relations at $z \sim 1.5 - 3.5$ from Sanders et al. (2021) in the gray shaded region and the relation at $z \sim 0 - 3.7$ from Tortora et al. (2022) in the purple shaded region. For MACS0647−JD, we scale the stellar mass by a factor of 0.92 and SFR by a factor of 0.94 accounting for the initial mass function from Kroupa (2002) to Chabrier (2003).

Figure 7. The mass-metallicity relation. MACS0647−JD (this work) determined using direct T_e method is shown in the red star. *(Top panel:)* We compare MACS0647−JD with some previous works on high redshift galaxies, including Nakajima et al. (2023, orange Xs and the dot-dashed line) at $4 < z < 10$, Heintz et al. (2023, the violet line) at $7 < z < 10$, Curti et al. (2023, the grey dashed line) at $6 < z < 10$, and Morishita et al. (2024, tiffany green triangles and the dot line) at $3 < z < 9.5$. For Nakajima et al. (2023) and Morishita et al. (2024), we show only galaxies derived from direct T_e. Shaded regions represent 1σ confidence interval of each fit. *(Bottom panel:)* We also compare MACS0647−JD to a number of theoretical predictions (Dayal et al. 2022; Ucci et al. 2023; Wilkins et al. 2023; Marszewski et al. 2024), as marked; the (green) contour shows the extent of the mass-metallicity relation allowed by the ASTRAEUS model (Ucci et al. 2023). For MACS0647−JD, Heintz et al. (2023), and Marszewski et al. (2024), we scale the stellar mass by a factor of 0.92 accounting for the initial mass function from Kroupa (2002) to Chabrier (2003) while we scale the stellar mass by a factor of 0.61 for Dayal et al. (2022) and Ucci et al. (2023) from Salpeter (1955) to Chabrier (2003).

$z \sim 10$ galaxy fortuitously lensed to be the brightest yet known, enabling detailed study.

JWST Cycle 3 program GTO 4528 (PI Isaak) will observe 13 targets with NIRSpec IFU, including MACS0647–JD with G395M. This will be promising to measure total line fluxes, improve the metallicity precision, disentangle contributions from components A and B, and measure any velocity difference to constrain the dynamical mass. Additionally, they could spectroscopically confirm companion C, which is not detected in our MIRI MRS data.

MIRI extends the ability of JWST to obtain direct metallicity measurements for galaxies at $z > 9.5$ with detections of [O III] $\lambda5008$. What we gain with MIRI is 100 Myr of cosmic time when direct metallicity measurements are still possible, pushing the limit from $z \sim 9.5$ ($\sim$500 Myr after the Big Bang) to $z \sim 11.1$ ($\sim$400 Myr). Beyond that redshift we will need to swap accurate direct methods for calibrated diagnostics. Even though these are less precise, this work demonstrates that such

diagnostics *can* be relied upon to measure metallicity in high-z systems like MACS0647−JD.

MIRI also delivers other important measurements, including star formation rate and ξ_{ion}, to higher redshifts $z > 11$, as shown with GHZ2/GLASS-z12 at $z = 12.33$ (Zavala et al. 2024).

6. ACKNOWLEDGMENTS

Facilities: JWST(NIRCam, NIRSpec, MIRI), HST(ACS, WFC3)

Software: STScI JWST pipeline; MSAEXP; GRIZLI (Brammer et al. 2022); ASTROPY (Astropy Collaboration et al. 2022, 2018, 2013); PIXEDFIT (Abdurro'uf et al. 2021, 2022); PYNEB (Luridiana et al. 2015); HII-CHI-MISTRY (Pérez-Montero 2014)

APPENDIX

REFERENCES

Abdurro'uf, Lin, Y.-T., Wu, P.-F., & Akiyama, M. 2021, ApJS, 254, 15, doi: 10.3847/1538-4365/abebe2

—. 2022, piXedfit: Analyze spatially resolved SEDs of galaxies, Astrophysics Source Code Library, record ascl:2207.033

Álvarez-Márquez, J., Colina, L., Marques-Chaves, R., et al. 2019, A&A, 629, A9, doi: 10.1051/0004-6361/201935594

Álvarez-Márquez, J., Colina, L., Crespo Gómez, A., et al. 2023a, arXiv e-prints, arXiv:2309.06319, doi: 10.48550/arXiv.2309.06319

Álvarez-Márquez, J., Crespo Gómez, A., Colina, L., et al. 2023b, A&A, 671, A105, doi: 10.1051/0004-6361/202245400

Andrews, B. H., & Martini, P. 2013, ApJ, 765, 140, doi: 10.1088/0004-637X/765/2/140

Argyriou, I., Glasse, A., Law, D. R., et al. 2023, A&A, 675, A111, doi: 10.1051/0004-6361/202346489

Asplund, M., Grevesse, N., Sauval, A. J., & Scott, P. 2009, ARA&A, 47, 481, doi: 10.1146/annurev.astro.46.060407.145222

Astropy Collaboration, Robitaille, T. P., Tollerud, E. J., et al. 2013, A&A, 558, A33, doi: 10.1051/0004-6361/201322068

Astropy Collaboration, Price-Whelan, A. M., Sipőcz, B. M., et al. 2018, AJ, 156, 123, doi: 10.3847/1538-3881/aabc4f

Astropy Collaboration, Price-Whelan, A. M., Lim, P. L., et al. 2022, ApJ, 935, 167, doi: 10.3847/1538-4357/ac7c74

Atek, H., Labbé, I., Furtak, L. J., et al. 2024, Nature, 626, 975, doi: 10.1038/s41586-024-07043-6

Böker, T., Beck, T. L., Birkmann, S. M., et al. 2023, PASP, 135, 038001, doi: 10.1088/1538-3873/acb846

Bouchet, P., García-Marín, M., Lagage, P. O., et al. 2015, PASP, 127, 612, doi: 10.1086/682254

Boyett, K., Trenti, M., Leethochawalit, N., et al. 2023, arXiv e-prints, arXiv:2303.00306, doi: 10.48550/arXiv.2303.00306

Brammer, G., Strait, V., Matharu, J., & Momcheva, I. 2022, grizli, 1.5.0, Zenodo, doi: 10.5281/zenodo.6672538

Bunker, A. J., Saxena, A., Cameron, A. J., et al. 2023, A&A, 677, A88, doi: 10.1051/0004-6361/202346159

Bushouse, H., Eisenhamer, J., Dencheva, N., et al. 2024, JWST Calibration Pipeline, 1.13.4, Zenodo, doi: 10.5281/zenodo.6984365

Campbell, A., Terlevich, R., & Melnick, J. 1986, MNRAS, 223, 811, doi: 10.1093/mnras/223.4.811

Castellano, M., Napolitano, L., Fontana, A., et al. 2024, arXiv e-prints, arXiv:2403.10238, doi: 10.48550/arXiv.2403.10238

Chabrier, G. 2003, PASP, 115, 763, doi: 10.1086/376392

Chan, B. M. Y., Broadhurst, T., Lim, J., et al. 2017, ApJ, 835, 44, doi: 10.3847/1538-4357/835/1/44

Coe, D., Zitrin, A., Carrasco, M., et al. 2013, ApJ, 762, 32, doi: 10.1088/0004-637X/762/1/32

Curti, M., Mannucci, F., Cresci, G., & Maiolino, R. 2020, MNRAS, 491, 944, doi: 10.1093/mnras/stz2910

Curti, M., Maiolino, R., Curtis-Lake, E., et al. 2023, arXiv e-prints, arXiv:2304.08516, doi: 10.48550/arXiv.2304.08516

Dayal, P., Ferrara, A., Sommovigo, L., et al. 2022, MNRAS, 512, 989, doi: 10.1093/mnras/stac537

de Graaff, A., Rix, H.-W., Carniani, S., et al. 2023, arXiv e-prints, arXiv:2308.09742, doi: 10.48550/arXiv.2308.09742

Díaz, A. I., Castellanos, M., Terlevich, E., & Luisa García-Vargas, M. 2000, MNRAS, 318, 462, doi: 10.1046/j.1365-8711.2000.03737.x

Dicken, D., García Marín, M., Shivaei, I., et al. 2024, arXiv e-prints, arXiv:2403.16686, doi: 10.48550/arXiv.2403.16686

Dopita, M. A., & Sutherland, R. S. 2003, Astrophysics of the diffuse universe, doi: 10.1007/978-3-662-05866-4

Ferruit, P., Jakobsen, P., Giardino, G., et al. 2022, A&A, 661, A81, doi: 10.1051/0004-6361/202142673

Fujimoto, S., Arrabal Haro, P., Dickinson, M., et al. 2023, arXiv e-prints, arXiv:2301.09482, doi: 10.48550/arXiv.2301.09482

Gaia Collaboration, Klioner, S. A., Lindegren, L., et al. 2022, A&A, 667, A148, doi: 10.1051/0004-6361/202243483

Gardner, J. P., Mather, J. C., Abbott, R., et al. 2023, arXiv e-prints, arXiv:2304.04869, doi: 10.48550/arXiv.2304.04869

Groves, B., Brinchmann, J., & Walcher, C. J. 2012, MNRAS, 419, 1402, doi: 10.1111/j.1365-2966.2011.19796.x

Heintz, K. E., Brammer, G. B., Giménez-Arteaga, C., et al. 2023, Nature Astronomy, 7, 1517, doi: 10.1038/s41550-023-02078-7

Hicks, E. K. S., Malkan, M. A., Teplitz, H. I., McCarthy, P. J., & Yan, L. 2002, ApJ, 581, 205, doi: 10.1086/344224

Hsiao, T. Y.-Y., Coe, D., Abdurro'uf, et al. 2023a, ApJL, 949, L34, doi: 10.3847/2041-8213/acc94b

Hsiao, T. Y.-Y., Abdurro'uf, Coe, D., et al. 2023b, arXiv e-prints, arXiv:2305.03042, doi: 10.48550/arXiv.2305.03042

Izotov, Y. I., Stasińska, G., Meynet, G., Guseva, N. G., & Thuan, T. X. 2006, A&A, 448, 955, doi: 10.1051/0004-6361:20053763

Jakobsen, P., Ferruit, P., Alves de Oliveira, C., et al. 2022, A&A, 661, A80, doi: 10.1051/0004-6361/202142663

Jones, O. C., Álvarez-Márquez, J., Sloan, G. C., et al. 2023, MNRAS, 523, 2519, doi: 10.1093/mnras/stad1609

Jung, I., Finkelstein, S. L., Arrabal Haro, P., et al. 2023, arXiv e-prints, arXiv:2304.05385, doi: 10.48550/arXiv.2304.05385

Kennicutt, Robert C., J. 1998, ARA&A, 36, 189, doi: 10.1146/annurev.astro.36.1.189

Kewley, L. J., & Dopita, M. A. 2002, ApJS, 142, 35, doi: 10.1086/341326

Kewley, L. J., & Ellison, S. L. 2008, ApJ, 681, 1183, doi: 10.1086/587500

Kroupa, P. 2002, Science, 295, 82, doi: 10.1126/science.1067524

Labiano, A., Argyriou, I., Álvarez-Márquez, J., et al. 2021, A&A, 656, A57, doi: 10.1051/0004-6361/202140614

Law, D. R., E. Morrison, J., Argyriou, I., et al. 2023, AJ, 166, 45, doi: 10.3847/1538-3881/acdddc

Libralato, M., Argyriou, I., Dicken, D., et al. 2024, PASP, 136, 034502, doi: 10.1088/1538-3873/ad2551

Luridiana, V., Morisset, C., & Shaw, R. A. 2015, A&A, 573, A42, doi: 10.1051/0004-6361/201323152

Mannucci, F., Cresci, G., Maiolino, R., Marconi, A., & Gnerucci, A. 2010, MNRAS, 408, 2115, doi: 10.1111/j.1365-2966.2010.17291.x

Marszewski, A., Sun, G., Faucher-Giguère, C.-A., Hayward, C. C., & Feldmann, R. 2024, arXiv e-prints, arXiv:2403.08853, doi: 10.48550/arXiv.2403.08853

Meena, A. K., Zitrin, A., Jiménez-Teja, Y., et al. 2023, ApJL, 944, L6, doi: 10.3847/2041-8213/acb645

Mingozzi, M., James, B. L., Berg, D. A., et al. 2024, ApJ, 962, 95, doi: 10.3847/1538-4357/ad1033

Morishita, T., Stiavelli, M., Grillo, C., et al. 2024, arXiv e-prints, arXiv:2402.14084, doi: 10.48550/arXiv.2402.14084

Nakajima, K., Ouchi, M., Isobe, Y., et al. 2023, ApJS, 269, 33, doi: 10.3847/1538-4365/acd556

Nicholls, D. C., Kewley, L. J., & Sutherland, R. S. 2020, PASP, 132, 033001, doi: 10.1088/1538-3873/ab6818

Oke, J. B. 1974, ApJS, 27, 21, doi: 10.1086/190287

Oke, J. B., & Gunn, J. E. 1983, ApJ, 266, 713, doi: 10.1086/160817

Osterbrock, D. E. 1989, Astrophysics of gaseous nebulae and active galactic nuclei

Papovich, C., Simons, R. C., Estrada-Carpenter, V., et al. 2022, ApJ, 937, 22, doi: 10.3847/1538-4357/ac8058

Patapis, P., Argyriou, I., Law, D. R., et al. 2024, A&A, 682, A53, doi: 10.1051/0004-6361/202347339

Peimbert, M. 1967, ApJ, 150, 825, doi: 10.1086/149385

Pérez-González, P. G., Barro, G., Rieke, G. H., et al. 2024, arXiv e-prints, arXiv:2401.08782, doi: 10.48550/arXiv.2401.08782

Pérez-Montero, E. 2014, MNRAS, 441, 2663, doi: 10.1093/mnras/stu753

Planck Collaboration, Aghanim, N., Akrami, Y., et al. 2020, A&A, 641, A6, doi: 10.1051/0004-6361/201833910

Reddy, N. A., Shapley, A. E., Sanders, R. L., et al. 2018, ApJ, 869, 92, doi: 10.3847/1538-4357/aaed1e

Rieke, G. H., Wright, G. S., Böker, T., et al. 2015, PASP, 127, 584, doi: 10.1086/682252

Rigby, J., Perrin, M., McElwain, M., et al. 2023, Publications of the Astronomical Society of the Pacific, 135, 048001, doi: 10.1088/1538-3873/acb293

Robertson, B. E., Furlanetto, S. R., Schneider, E., et al. 2013, ApJ, 768, 71, doi: 10.1088/0004-637X/768/1/71

Salpeter, E. E. 1955, ApJ, 121, 161, doi: 10.1086/145971

Sanders, R. L., Shapley, A. E., Topping, M. W., Reddy, N. A., & Brammer, G. B. 2024, ApJ, 962, 24, doi: 10.3847/1538-4357/ad15fc

Sanders, R. L., Shapley, A. E., Jones, T., et al. 2021, ApJ, 914, 19, doi: 10.3847/1538-4357/abf4c1

Schaerer, D. 2003, A&A, 397, 527, doi: 10.1051/0004-6361:20021525

Stanway, E. R., & Eldridge, J. J. 2018, MNRAS, 479, 75, doi: 10.1093/mnras/sty1353

Tang, M., Stark, D. P., Chen, Z., et al. 2023, arXiv e-prints, arXiv:2301.07072, doi: 10.48550/arXiv.2301.07072

Tortora, C., Hunt, L. K., & Ginolfi, M. 2022, A&A, 657, A19, doi: 10.1051/0004-6361/202140414

Tremonti, C. A., Heckman, T. M., Kauffmann, G., et al. 2004, ApJ, 613, 898, doi: 10.1086/423264

Ucci, G., Dayal, P., Hutter, A., et al. 2023, MNRAS, 518, 3557, doi: 10.1093/mnras/stac2654

Vanzella, E., Loiacono, F., Bergamini, P., et al. 2023, A&A, 678, A173, doi: 10.1051/0004-6361/202346981

Wells, M., Pel, J. W., Glasse, A., et al. 2015, PASP, 127, 646, doi: 10.1086/682281

Wilkins, S. M., Feng, Y., Di-Matteo, T., et al. 2016, MNRAS, 458, L6, doi: 10.1093/mnrasl/slw007

Wilkins, S. M., Vijayan, A. P., Lovell, C. C., et al. 2023, MNRAS, 518, 3935, doi: 10.1093/mnras/stac3281

Wright, G. S., Wright, D., Goodson, G. B., et al. 2015, PASP, 127, 595, doi: 10.1086/682253

Wright, G. S., Rieke, G. H., Glasse, A., et al. 2023, PASP, 135, 048003, doi: 10.1088/1538-3873/acbe66

Zavala, J. A., Castellano, M., Akins, H. B., et al. 2024, arXiv e-prints, arXiv:2403.10491, doi: 10.48550/arXiv.2403.10491

Zitrin, A., Fabris, A., Merten, J., et al. 2015, ApJ, 801, 44, doi: 10.1088/0004-637X/801/1/44